

Lattice Dynamics and Electron–Phonon Coupling in Double Perovskite $\text{Cs}_2\text{NaFeCl}_6$

Bin Zhang,* Johan Klarbring, Fuxiang Ji, Sergei I. Simak, Igor A. Abrikosov, Feng Gao, Galyna Yu Rudko, Weimin M. Chen, and Irina A. Buyanova*



Cite This: *J. Phys. Chem. C* 2023, 127, 1908–1916



Read Online

ACCESS |



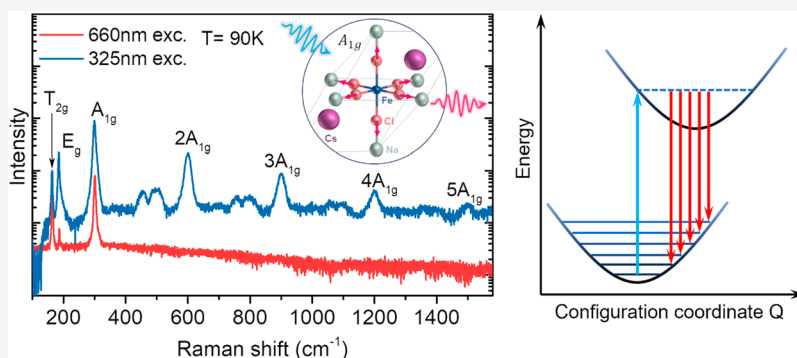
Metrics & More



Article Recommendations



Supporting Information



ABSTRACT: Phonon–phonon and electron/exciton–phonon coupling play a vitally important role in thermal, electronic, as well as optical properties of metal halide perovskites. In this work, we evaluate phonon anharmonicity and coupling between electronic and vibrational excitations in novel double perovskite $\text{Cs}_2\text{NaFeCl}_6$ single crystals. By employing comprehensive Raman measurements combined with first-principles theoretical calculations, we identify four Raman-active vibrational modes. Polarization properties of these modes imply $Fm\bar{3}m$ symmetry of the lattice, indicative for on average an ordered distribution of Fe and Na atoms in the lattice. We further show that temperature dependence of the Raman modes, such as changes in the phonon line width and their energies, suggests high phonon anharmonicity, typical for double perovskite materials. Resonant multiphonon Raman scattering reveals the presence of high-lying band states that mediate strong electron–phonon coupling and give rise to intense nA_{1g} overtones up to the fifth order. Strong electron–phonon coupling in $\text{Cs}_2\text{NaFeCl}_6$ is also concluded based on the Urbach tail analysis of the absorption coefficient and the calculated Fröhlich coupling constant. Our results, therefore, suggest significant impacts of phonon–phonon and electron–phonon interactions on electronic properties of $\text{Cs}_2\text{NaFeCl}_6$, important for potential applications of this novel material.

1. INTRODUCTION

Lead halide perovskites have gained a significant attention over the past decade due to their interesting fundamental physical properties and rapid developments of perovskite-based optoelectronic and photonic devices, such as solar cells and color-tunable light-emitting diodes (LEDs).^{1–4} For example, an external quantum efficiency of perovskite LEDs fabricated through a simple and low-cost solution process has increased to over 20% owing to their exceptional defect tolerance, rivalling commercial LEDs from conventional III–V semiconductors and colloidal quantum dots.^{5,6} Despite the remarkable optoelectronic performance, the toxicity of lead and the lack of stability against prolonged illumination, moisture, and heat in operational environments limit their large-scale deployment.^{7,8} To circumvent these issues inherent to the lead halide perovskites, increasing efforts have been devoted to developing lead-free alternative compounds with better stability and nontoxicity. Here, an emerging and

promising strategy is heterovalent substitution of Pb^{2+} with one monovalent (B^I) and one trivalent (B^{III}) metal cation. This gives rise to a so-called double perovskite architecture with a general stoichiometric formula $A_2B^IB^{III}X_6$, where alternating metal cations B^I and B^{III} are octahedrally coordinated by six halide anions X , whereas the monovalent cations A are embedded in interstitial positions of the octahedral framework. This architecture opens up unprecedented possibilities to engineer structural and electronic properties of these lead-free materials for photonic applications, including solar cells,^{9–13} X-

Received: October 25, 2022

Revised: January 5, 2023

Published: January 19, 2023



ray detectors,¹⁴ and warm-white LEDs,¹⁵ through judicious combination of various A-, B-, or X-site elements and alloying.^{16–21} Moreover, by substituting a metal cation by a magnetic impurity, e.g., a transition metal ion, double perovskite materials may acquire a magnetic response, which is promising for future spintronic applications.²¹

One of the promising lead-free double perovskite materials is the novel Cs₂NaFeCl₆ compound. Most recent studies²² have shown that this material is thermally stable and exhibits exceptionally strong and completely reversible thermochromism within a wide temperature range that is caused by a strong temperature dependence of its bandgap energy.^{22,23} Since its onset energy of optical absorption lies within the visible spectral range (at around 2.1 eV at room temperature), Cs₂NaFeCl₆ could potentially be used in displaying devices, including smart windows, visual thermometers, and thermal sensors. Furthermore, the presence of transition-metal Fe³⁺ ions with an unpaired electron spin suggests interesting magnetic properties attractive for spintronic applications. Exploiting Cs₂NaFeCl₆ for practical applications requires a better understanding of its fundamental physical properties, including lattice dynamics and electron–phonon interactions, which are known to be of profound importance for double perovskites but have so far been scarcely studied and explored for this recently synthesized compound. Unlike the conventional inorganic covalent semiconductors (e.g., GaAs), a soft lattice of halide perovskites usually displays large anharmonicity due to phonon–phonon interactions and is also deformable in the presence of charge carriers due to strong electron–phonon interactions.^{15,24} The phonon anharmonicity can shorten phonon lifetimes and cause a finite phonon mean free path, thereby limiting thermal transport performance of the material.²⁵ Strong electron–phonon coupling is expected to lead to lattice distortion/displacement that can disturb a periodic potential experienced by charge carriers, giving rise to polaronic effects, broadening, and a Stokes shift of light emission, and also impacts carrier mobility.^{26–29} All of these effects could also be affected by the ordering of B cations in the lattice.^{30,31} Therefore, understanding lattice dynamics and electron–phonon interactions in Cs₂NaFeCl₆ is of great importance not only for fundamental insights but also for future optoelectronic and spintronic applications.

In this work, we fabricate high-quality double perovskite Cs₂NaFeCl₆ single crystals and examine their vibronic properties and electron–phonon interactions by combining in-depth experimental studies based on polarization-resolved and temperature-dependent Raman and absorption measurements with first-principles calculations.

2. METHODS

Crystal Growth. The investigated samples were millimeter-sized Cs₂NaFeCl₆ single crystals. For single crystal synthesis, solid CsCl (168.36 mg, 1.00 mmol), NaCl (29.22 mg, 0.5 mmol), and FeCl₃ (81.1 mg, 0.5 mmol) were dissolved in 7 mL of 37% HCl and then transferred into a 25 cm³ Teflon-lined autoclave. The autoclave was sealed, placed in the oven, and then heated to 180 °C for 12 h. After slowly cooling down to room temperature at a rate of 1 °C/h, red Cs₂NaFeCl₆ single crystals were formed.

Optical Measurements. Raman scattering measurements were performed using a confocal Horiba Jobin-Yvon HR800 system in a back scattering geometry. A solid-state 660 nm laser was used as an excitation source during polarization-

resolved Raman experiments. To select a desired polarization of the excitation light, a fixed linear polarizer and a rotatable halfwave plate were placed between the light source and surface of the sample, which was mounted in a variable temperature He(N₂)-flow cryostat. The excitation power was set to be below 1 mW/μm² to avoid heating effects. The induced Raman scattering signal was collected with a long working distance objective (50×, NA = 0.5) and registered by a high-resolution grating (1800/3600 g/mm) monochromator equipped with a charge-coupled device (CCD) detector. Polarization of the scattered light was selected to be either parallel or orthogonal to that of the excitation light by using a halfwave plate coupled with a fixed linear analyzer. For ultraviolet (UV) Raman spectroscopy, the excitation source was switched to a He–Cd 325 nm laser. During transmission measurements, a tungsten halogen lamp was used as a light source, whereas a grating monochromator equipped with a photomultiplier was employed to register the transmitted light.

First-Principles Simulations. The density functional theory (DFT) simulations were carried out using the Vienna Ab Initio Simulation Package (VASP).^{32–34} We used the PBEsol³⁵ exchange–correlation functional and an effective Hubbard *U* correction of *U*_{eff} = 3 eV on the Fe(d) states in the form according to Dudarev et al.³⁶ SCPH calculations were employed as implemented in the ALAMODE code.^{37–39} Full details on the methodology and specific settings of both the DFT and phonon calculations are provided in the [Supporting Information](#).

3. EXPERIMENTAL RESULTS AND DISCUSSION

3.1. General Vibrational Properties and Phonon Anharmonicity. Figure 1a shows a characteristic top-view optical image of the investigated Cs₂NaFeCl₆ double perovskite single crystals (SCs). The crystal exhibits a truncated octahedron geometry typical for this material with top and bottom planes and six sidewall facets belonging to the {111} plane family.^{23,40} The well-defined crystal shape allows us to identify Raman-active phonon modes using polarization-resolved Raman spectroscopy. The experimental configuration for such measurements is shown in the right panel of Figure 1a. The incident light and induced backscattering Raman signal propagate in the direction normal to the top crystal plane, coinciding with the crystallographic [111] direction, whereas the *y* axis is set along one edge of the triangular top facet, i.e., the [110] crystallographic direction. Representative low-temperature (*T* = 90 K) Raman spectra in four polarization configurations, i.e., parallel ($z(x, x)\bar{z} \leftrightarrow z(y, y)\bar{z}$) and perpendicular ($z(x, y)\bar{z} \leftrightarrow z(y, x)\bar{z}$) geometries for the polarization vectors of incoming and scattered light, are found to contain several Raman peaks as shown in Figure 1b. Over the temperature range of 80–300 K, the Cs₂NaFeCl₆ SC was shown to exhibit a cubic phase. The overall lattice symmetry depends on the ordering of Na and Fe cations and changes from the *Fm* $\bar{3}$ *m* symmetry space group for the perfectly ordered Cs₂NaFeCl₆ with alternating [NaCl₆] and [FeCl₆] octahedra to *Pm* $\bar{3}$ *m* for their fully random distribution.⁴¹ A careful group-theory analysis shows that the first-order Raman scattering is forbidden in the latter case, while the zone-center Raman-active modes in the ordered material can be classified as the following irreducible representation: *A*_{1g} + *E*_g + *T*_{2g} + *T*_{2g-Cs}. Here *T*_{2g-Cs} is the external translational mode of the Cs⁺ lattice, and *A*_{1g}, *E*_g, and *T*_{2g} are the internal modes of the octahedra.^{42,43} Therefore, the observation of intense Raman

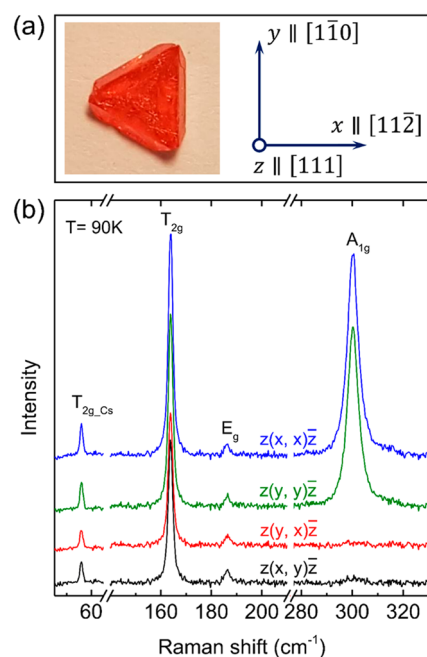


Figure 1. (a) Schematics of the geometry used in polarization-resolved Raman measurements. Left: a top-view optical image of a typical double perovskite $\text{Cs}_2\text{NaFeCl}_6$ single crystal studied in this work. Right: the utilized Cartesian coordinate system, where z axis is chosen to be perpendicular to the top and bottom surfaces of the crystal, whereas y axis is oriented along one edge of the top triangular surface. (b) Representative low-temperature ($T = 90$ K) Raman spectra recorded under the 660 nm light excitation. The polarization directions of incident excitation light and Raman scattered light are set according to the corresponding Porto notations. The spectra are offset vertically for clarity.

scattering involving four phonon modes implies a regular alternating distribution of the Fe and Na atoms in the lattice with the $Fm\bar{3}m$ symmetry. According to the selection rules for the Raman scattering in the backscattering geometry along the $[111]$ crystal orientation, the A_{1g} phonon mode is only allowed in the parallel configurations; the T_{2g} phonon mode has a larger intensity in the parallel geometries with respect to the perpendicular ones; whereas the intensity of the E_g phonon mode is expected to be the same in both parallel and crossed configurations (see also [Supporting Information](#)). Experimentally, the mode peaked at 300.3 cm^{-1} only appears in parallel polarization geometries and, therefore, obeys the A_{1g} symmetry. The feature located at around 186.2 cm^{-1} can be assigned to the E_g phonon mode due to its configuration-independent intensity, whereas the polarization pattern of the two remaining modes indicates their T_{2g} symmetry. We therefore attribute the high frequency T_{2g} phonon mode near 163.8 cm^{-1} to bending vibrations of the octahedra cages, whereas the low frequency mode at 56 cm^{-1} is assigned to the translational lattice motion of Cs^+ ions. The suggested mode assignment is further confirmed by the performed density functional theory (DFT) calculations to be discussed below.

Further information on vibrational properties of the $\text{Cs}_2\text{NaFeCl}_6$ SCs can be obtained from temperature-dependent Raman measurements. The results of these measurements are summarized in [Figure 2](#). First of all, we note that the four Raman modes studied in this work could be detected without any extra features within the temperature range of 77–300 K, indicating preservation of the $Fm\bar{3}m$ lattice symmetry and,

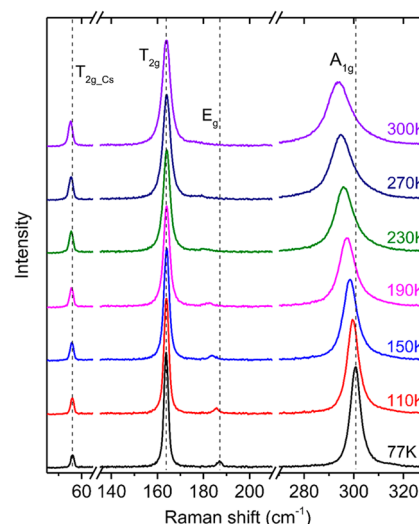


Figure 2. Unpolarized Raman spectra measured at several temperatures ranging from 77 to 300 K. For a better overview, the spectra are offset vertically. The vertical dashed lines are a guide to the eye.

therefore, the absence of an order–disorder transition up to room temperature. However, substantial broadening of the Raman peaks, which is most pronounced for the A_{1g} mode, is observed. This is accompanied by a strong temperature-induced red shift of the A_{1g} and E_g modes, while both T_{2g} and T_{2g_Cs} modes remain practically fixed in energy.

Having experimentally identified the symmetry and origin of all active phonon modes, as well as their temperature dependence, we proceed to gain in-depth physical insight into the microscopic origin of the phonon modes by theoretically calculating the vibrational spectrum of $\text{Cs}_2\text{NaFeCl}_6$. [Figure 3a](#) shows the computed phonon dispersion and density of states (DOS) at 100 K. The set of low-energy modes up to $\sim 85\text{ cm}^{-1}$ corresponds primarily to Cs motion and octahedral tilting vibrations, whereas the modes around $\sim 100\text{ cm}^{-1}$ and between ~ 125 and 150 cm^{-1} are primarily bending and scissoring motions of the octahedra. The modes higher than 150 cm^{-1} correspond to different types of Fe–Cl/Na–Cl stretching motion. The four Raman active modes are indicated in the dispersion, and we note a satisfactory agreement with our experimentally measured frequencies, with a slight underestimation (at most $\sim 6\%$) for the high-frequency modes (see [Table 1](#)).

Next, we consider the effect of temperature on the Raman-active phonon modes. [Figure 3b](#) compares the theoretically deduced frequency shifts with the experimental values (the blue triangles). We show two separate theoretical curves. For the first theoretical curve (see the orange curves), the quasi-harmonic (QH) approximation is applied, where the temperature-induced frequency shift is evaluated only by expanding the volume of the structure, following the measured thermal expansion.²² Even though this approximation can reasonably describe the experimentally measured frequency shifts of the A_{1g} , E_g , and T_{2g_Cs} modes, it predicts a strong downward shift of the T_{2g} mode (see the orange squares in [Figure 3b](#)), which is not observed experimentally. For the second theoretical curve (see the green curves), we include, in addition to the volumetric thermal expansion, the effect of intrinsic anharmonicity, i.e., phonon–phonon interactions, using a self-consistent phonon (SCPH) methodology^{37–39} (see also

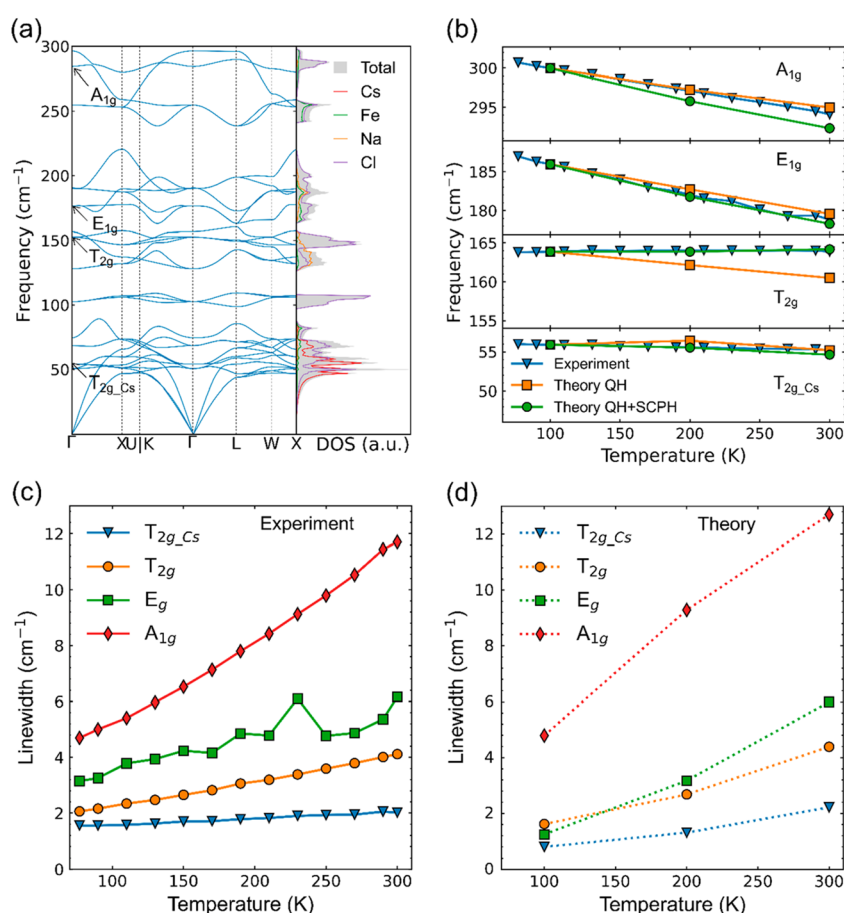


Figure 3. (a) DFT calculated phonon band dispersion curves (the left panel) and total density of states (the right panel). The Raman active modes are marked according to their symmetry. (b) Experimentally measured and theoretically simulated shifts of the phonon frequencies for the four Raman active phonon modes as a function of measurement temperature. The orange squares and green circles are the results of calculations within the QH and QH+SCPH approximations, respectively. The theoretical curves have been shifted to match the measured frequencies at 100 K, in order to compare the temperature dependence more clearly. Measured (c) and calculated (d) line widths of the Raman active modes as a functional of temperature.

Table 1. Experimentally Measured Phonon Frequencies (exp.) of the Four Raman Active Modes and Theoretically Expected Phonon Frequencies Calculated by Two Computational Methodologies: the Quasi-Harmonic (QH) Approximation and Self-Consistent Phonon (SCPH) + QH Approximation

mode (symm.)	mode frequency (cm ⁻¹)		
	exp. (110 K)	QH (100 K)	SCPH + QH(100 K)
T_{2g_Cs}	55.9	54.3	54.2
T_{2g}	163.9	150.7	152.6
E_g	185.6	177.7	176.4
A_{1g}	299.7	286.1	284.4

Methods and Supporting Information). The corresponding results are shown by the green circles in Figure 3b. Now the good agreement between the experimental and theoretical results is achieved for all Raman-active modes, which shows that explicitly including phonon–phonon interactions is required to qualitatively reproduce the correct temperature-induced variations of the phonon frequencies determined from our measurements.

We now discuss temperature-dependent broadening of the Raman modes. The line width Γ of a phonon mode is linked

with the phonon lifetime τ by $\Gamma \sim 1/\tau$. In general, there are two primary sources of the phonon damping, i.e., defects/disorder and intrinsic phonon anharmonicity. Phonon lifetime limited by defects/disorder is known to be temperature independent and, therefore, could be responsible for the phonon line width at low temperatures. On the other hand, the intrinsic anharmonicity, that is, decay of a higher-energy phonon into several phonons with low energies, is usually activated with increasing temperature. The measured and calculated line width of the Raman-active modes as a function of temperature is shown in Figure 3c and d, respectively. We note a qualitatively good agreement between theory and experiment. Since the calculated line widths only take into account the intrinsic phonon anharmonicity, this is likely the primary source of the phonon broadening observed in our measurements. This is probably not surprising considering that both single and double halide perovskites are known to be highly anharmonic materials.^{24,25} From Figure 3c is also noticeable that the A_{1g} line width is significantly broader than that of the other modes at low temperatures and also increases much faster with increasing temperature. This suggests that this mode is more sensitive to phonon–phonon interactions than the other Raman active modes.

3.2. Multiphonon Raman Scattering and Electron–Phonon Coupling. Furthermore, our experiments show that additional phonon modes appear in Raman spectra when the excitation photon energy ($h\omega_{\text{exc}}$) is tuned above the $\text{Cs}_2\text{NaFeCl}_6$ bandgap (E_g). Most surprisingly, this effect becomes especially pronounced under the condition of $h\omega_{\text{exc}} \gg E_g$. This finding is illustrated in the Supporting Information and Figure 4a, which shows a representative Raman spectrum

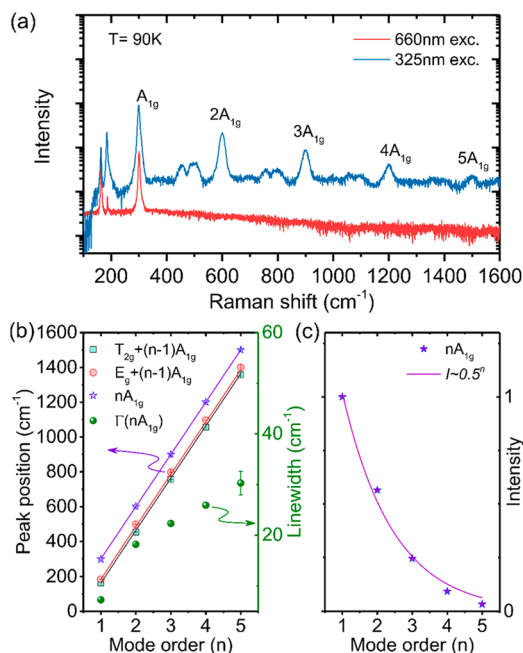


Figure 4. (a) Experimental Raman scattering spectra recorded at $T = 90$ K in a wide frequency range. The blue and red curves represent the spectra measured under the 325 and 660 nm light excitation, respectively. Notations of nA_{1g} modes label overtones of the A_{1g} mode in accordance with the mode order n . (b) The measured frequency positions (symbols) of the nA_{1g} overtones and the combination modes of $T_{2g} + (n-1)A_{1g}$ and $E_g + (n-1)A_{1g}$ obtained by fitting the experimental data with multiple Lorentzian functions. The solid lines are linear fits of these data with the same slope of 300.4 cm^{-1} . The green filled spheres show the line width of the A_{1g} overtones as a function of the mode order n . (c) Relative intensities (I) of the nA_{1g} overtones (symbols) deduced from (a). The solid curve is the best fit to the experimental data with the $I \sim 0.5^n$ function.

(the blue curve) recorded at 90 K under UV excitation with $h\omega_{\text{exc}} = 3.815 \text{ eV}$ (or 325 nm). For comparison, we also show a Raman spectrum detected under 660 nm excitation, i.e., under below bandgap excitation with $h\omega_{\text{exc}} = 1.879 \text{ eV}$ (the red curve). (Note that the bandgap energy of $\text{Cs}_2\text{NaFeCl}_6$ at 90 K is 2.482 eV.) It is apparent that four additional sets of lines, each containing a strong peak accompanied by two weaker features at its lower-energy side, appear under the UV excitation, suggesting involvement of resonance effects. The frequency and line width of these modes can be extracted by fitting the Raman spectrum with multiple-Lorentzian functions. Since no additional high-energy lattice vibrations are expected from the calculated phonon DOS, these high-frequency modes should originate from higher order phonon processes. The Raman shift of the dominant high-frequency modes is found to display a linear dependence on the mode order n with an equal spacing between the neighboring modes of 300.4 cm^{-1} , which is very close to the first-order frequency of the A_{1g} vibrations

(see Figure 1b). These modes, therefore, represent a multiphonon progression of the A_{1g} mode. The two weaker high-frequency features are found to be spaced by multiples of 300.4 cm^{-1} from the first order E_g and T_{2g} modes and, therefore, stem from the combination modes $E_g + (n-1)A_{1g}$ and $T_{2g} + (n-1)A_{1g}$, respectively. The spacing between the high-order harmonics is very close to the energy of the first-order A_{1g} mode, which suggests primarily involvement of the zone-center phonons in the multiphonon process. Some contributions from the zone-edge vibrations cannot be ruled out, however, considering flatness of the A_{1g} dispersion shown in Figure 3a.

The line width of the strong A_{1g} overtones is found to increase with increasing overtone order, as shown by the green filled spheres in Figure 4b. This suggests that the multiphonons peaks stem from resonant Raman scattering involving real states.^{44,45} Moreover, the overtone intensity (I) decreases with increasing mode order following the relation of $I \sim P^n$, which indicates that the n -order Raman process is a result of a sequential emission of n phonons.⁴⁶ Here P denotes the probability of scattering by one A_{1g} phonon that is determined by electron–phonon interaction. The best fit to the experimental data yields $P = 0.5 \pm 0.03$. This value is significantly higher than that characteristic for conventional Raman scattering processes, where the intensity of n -th overtone is expected to be several orders of magnitude lower than that of the $(n-1)$ th overtone due to a weak electron–phonon interaction.⁴⁶ The observation of the intense overtones (up to 5th order!), therefore, suggests strong electron–phonon coupling in $\text{Cs}_2\text{NaFeCl}_6$.

High-order resonant Raman scattering under above bandgap excitation has been observed in resonant Raman spectra of single and double perovskite materials, such as CsPbBr_3 ⁴⁵ and $\text{Cs}_2\text{Ag}_{0.4}\text{Na}_{0.6}\text{InCl}_6$,⁴⁷ and discussed in terms of polarons and self-trapped excitons. In this case, the strong electron–phonon interaction can locally deform crystal lattice in the vicinity of a photoexcited carrier leading to its self-trapping. Due to this local distortion, the excited electronic state has a different atomic coordinate than the ground state. If the excitation photon energy is sufficient for an optical transition between the ground and excited states, i.e., higher than the bandgap energy, multiphonon Raman scattering promoted by the Franck–Condon mechanism is activated. In the systems with a large Stokes shift between the ground and excited states, amplitude of the n -phonon resonant Raman scattering becomes proportional to the first order of the electron–phonon interaction, greatly enhancing intensities of the phonon overtones.^{37,48} We note, however, that such Raman resonances induced by self-trapped excitons were detected in perovskites when the excitation photon energy was only slightly higher than the bandgap energy.^{45,47} In our case, however, the high-order phonon modes are pronounced when $h\omega_{\text{exc}}$ is equal to 3.815 eV, i.e., exceeds the bandgap energy by about 1.3 eV. This suggests that the monitored resonance involves high-energy conduction- and/or valence-band states that are located well above their respective band edges. We note that the peak position of the Raman resonance could be slightly below 3.815 eV, as follows from the performed temperature-dependent measurements (see the Supporting Information). According to the performed DFT calculations, several high-energy conduction and valence band states with flat dispersion can give rise to resonant light absorption at around 3.815 eV and, therefore, could potentially be involved in the observed Raman

resonance (see the Supporting Information). A similar effect was also observed in $\text{Cs}_2\text{AgBiBr}_6$,²⁷ suggesting that it can be common for double perovskites. Though the exact origin of the states involved in the Raman resonance cannot be singled out from the present study, we note that strong multiphonon resonant Raman scattering under above bandgap excitation was also previously observed in LaMnO_3 and was attributed to the formation of self-trapped excitons that stem from orbital states (the so-called “orbiton”).^{37,48}

Further information regarding electron–phonon interactions in $\text{Cs}_2\text{NaFeCl}_6$ can be obtained by implementing the Urbach analysis⁴⁹ to the temperature-dependent absorption coefficient. It is known that in a wide variety of materials ranging from topologically disordered glasses^{50,51} to pure single crystals,⁵² the optical absorption coefficient α exhibits an exponential tail near the fundamental absorption edge that can be described by the following empirical equation:

$$\alpha = \alpha_0 \exp\left(-\sigma \frac{(E_0 - E)}{k_B T}\right) \quad (1)$$

Here k_B is the Boltzmann constant, T is the measurement temperature, and α_0 is the absorption coefficient at the convergence energy position $E = E_0$ termed as the Urbach focus. σ denotes the steepness parameter that together with $k_B T$ reflects the slope of the Urbach tail on a logarithmic scale. As expected from eq 1, measured spectral dependences of the absorption coefficient in the studied samples at each temperature obey a linear function if displayed in coordinates $\ln \alpha$ versus E , whereas extrapolations of these dependences to higher energy converge at the same energy $E_0 = 2.697$ eV, see Figure 5a. By fitting the low-energy tail of the absorption spectra with eq 1, we can then extract the steepness parameter, shown by symbols in Figure 5b. The steepness parameter $\sigma(T)$ varies with temperature as^{53,54}

$$\sigma(T) = \frac{k_B T}{E_U} = \sigma_0 \frac{2k_B T}{\hbar \nu_p} \tanh\left(\frac{\hbar \nu_p}{2k_B T}\right) \quad (2)$$

where E_U is the Urbach energy and $\hbar \nu_p$ represents the characteristic energy of phonons participating in the formation of the optical absorption edge. σ_0 is the temperature-independent steepness constant, which is inversely proportional to the strength of exciton–phonon interaction. As shown in Figure 5b, $\sigma(T)$ increases with temperature until the saturation value σ_0 is reached at high temperatures. The best fit to the steepness parameter $\sigma(T)$ by eq 2 yields $\hbar \nu_p = 22.7$ meV and $\sigma_0 = 0.23$. Here, the $\hbar \nu_p$ is not equal to any specific phonon energy in the Raman spectrum but is very close to an average value of the phonon energies, suggesting that all phonon modes are involved. Importantly, the magnitude of σ_0 enables us to evaluate the interaction of charge carriers with lattice vibrations.^{26,55} Following the theory of Toyozawa et al., free exciton becomes spatially localized by the surrounding lattice distortion of its own creation (i.e., a self-induced polaronic potential well) due to strong short-range electron–phonon interaction, if the steepness parameter σ_0 is below the threshold value $\sigma_c = 1.64$ for a three-dimensional cubic lattice.^{26,56,57} The extracted steepness constant $\sigma_0 = 0.23$ is apparently smaller than σ_c , which indicates that the formation of self-trapped excitons and small polarons is likely. We note that this value is even smaller than that of a sister double perovskite $\text{Cs}_2\text{AgBiBr}_6$ ($\sigma_0 = 0.56$),⁵⁸ indicating $\text{Cs}_2\text{NaFeCl}_6$

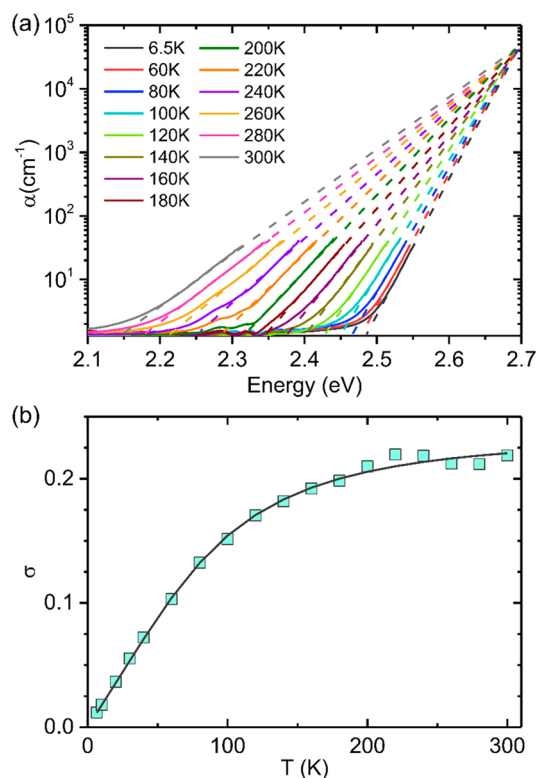


Figure 5. (a) Absorption coefficient measured at various temperatures (solid lines) as a function of photon energy. The dashed lines are expected energy dependences of the absorption tail by the Urbach rule, which converge at a single bundle point at 2.697 eV. (b) Temperature-dependent steepness parameter σ (symbols) extracted from the best fit of the experimental data shown in (a) by eq 1. The solid line represents the best fit of the calculated steepness parameter by eq 2, with $\sigma_0 = 0.23$ and $\hbar \nu_p = 0.023$ eV.

possesses a stronger short-range electron phonon interaction. Such strong electron–phonon interaction in $\text{Cs}_2\text{NaFeCl}_6$ may contribute to the extremely low carrier mobility ($\mu \sim 1.06$ cm² V^{−1} s^{−1}) in this material, as reported previously.²³

To further corroborate the presence of small polarons, we calculate the dimensionless Fröhlich coupling constant^{59,60}

$$\alpha_{\text{Fr}} = \frac{1}{4\pi\epsilon_0} \frac{1}{2} \left(\frac{1}{\epsilon_\infty} - \frac{1}{\epsilon_s} \right) \frac{e^2}{\hbar\Omega} \left(\frac{2m_b\Omega}{\hbar} \right)^{1/2} \quad (3)$$

where ϵ_∞ and ϵ_s are the optical and static dielectric constants, respectively; m_b is the electron band effective mass; Ω is an effective phonon angular frequency; e , \hbar , ϵ_0 are the electron charge, the reduced Planck constant; and the free space permittivity, respectively. We obtain a value of $\alpha_{\text{Fr}} = 7.11$ for electron polarons, which is much larger than that commonly found for halide perovskites,⁶¹ especially in comparison with the previously calculated values for other halide double perovskites, e.g., $\alpha_{\text{Fr}} = 2.54$ for $\text{Cs}_2\text{AgBiBr}_6$,²⁷ $\alpha_{\text{Fr}} = 2.82$ for $\text{Cs}_2\text{AgBiCl}_6$,⁶² and $\alpha_{\text{Fr}} = 1.99$ for $\text{Cs}_2\text{AgInCl}_6$.⁶² This puts $\text{Cs}_2\text{NaFeCl}_6$ into the strong polaron coupling regime, where the self-localization of electrons, i.e., the formation of small polarons, is likely. We note that this large value of α_{Fr} is a direct consequence of the large carrier effective mass in the conduction band, which is made up of highly localized bands of primarily Fe(d) character (Figure S4). Indeed, the remaining parameters entering α_{Fr} are comparable to those

of the other halide double perovskites mentioned above (see Table S2). We would like to stress that the value of the effective mass and thus the precise value of α_{Fr} is sensitive to the theoretical treatment of the electronic structure of the system, as briefly discussed in the Supporting Information.

4. CONCLUSION

In summary, we have carried out a detailed investigation of phonon–phonon and electron–phonon interactions in highly stable lead-free double perovskite $\text{Cs}_2\text{NaFeCl}_6$ single crystals by utilizing temperature-dependent Raman and optical absorption spectroscopy. By combining the polarization-resolved Raman spectroscopy and first-principle calculations, the origin and symmetry of four phonon modes active in Raman scattering are clearly identified, that is, one external translational mode of the Cs^+ lattice with T_{2g} symmetry and three internal modes of the octahedra corresponding to A_{1g} , E_g , and T_{2g} symmetries. We further show that the experimentally observed thermal behavior of the Raman-active modes, such as changes in their line widths and energies, could only be reproduced theoretically by explicitly including phonon anharmonicity, typical for this class of materials. It is also found that intense higher-order Raman scattering modes due to nA_{1g} overtones (up to the fifth order!) can be detected under above-bandgap excitation with $h\omega_{\text{exc}} = 3.815$ eV (or 325 nm). This is attributed to a resonant Raman scattering process that involves high-lying band states mediating strong electron–phonon coupling. Strong electron–phonon coupling, which may lead to the formation of small polarons and self-trapped excitons in $\text{Cs}_2\text{NaFeCl}_6$, is also concluded based on the steepness parameter extracted from a detailed Urbach analysis of the low-energy tail of the absorption spectra measured at different temperatures. This conclusion is further corroborated by the first-principles calculations, which find that the Fröhlich coupling constant in $\text{Cs}_2\text{NaFeCl}_6$ substantially exceeds that in other double perovskites, due to the large electron effective mass in this material. Our study, therefore, shows that phonon–phonon and electron–phonon interactions play an important role in $\text{Cs}_2\text{NaFeCl}_6$ and need to be taken into account when analyzing physical properties of this novel material, ranging from electronic and optical properties to thermal properties, key to a variety of future device application areas.

■ ASSOCIATED CONTENT

SI Supporting Information

The Supporting Information is available free of charge at <https://pubs.acs.org/doi/10.1021/acs.jpcc.2c07493>.

Raman selection rules in $\text{Cs}_2\text{NaFeCl}_6$, Urbach tail analysis, and computational details (PDF)

■ AUTHOR INFORMATION

Corresponding Authors

Bin Zhang – Department of Physics, Chemistry and Biology, Linköping University, Linköping SE-58183, Sweden; orcid.org/0000-0001-7862-2377; Email: bin.zhang@liu.se

Irina A. Buyanova – Department of Physics, Chemistry and Biology, Linköping University, Linköping SE-58183, Sweden; orcid.org/0000-0001-7155-7103; Email: irina.bouianova@liu.se

Authors

Johan Klarbring – Department of Physics, Chemistry and Biology, Linköping University, Linköping SE-58183, Sweden

Fuxiang Ji – Department of Physics, Chemistry and Biology, Linköping University, Linköping SE-58183, Sweden; Department of Physics and Astronomy, Uppsala University, Uppsala SE-75120, Sweden

Sergei I. Simak – Department of Physics, Chemistry and Biology, Linköping University, Linköping SE-58183, Sweden; Department of Physics and Astronomy, Uppsala University, Uppsala SE-75120, Sweden

Igor A. Abrikosov – Department of Physics, Chemistry and Biology, Linköping University, Linköping SE-58183, Sweden

Feng Gao – Department of Physics, Chemistry and Biology, Linköping University, Linköping SE-58183, Sweden; orcid.org/0000-0002-2582-1740

Galyna Yu Rudko – Department of Physics, Chemistry and Biology, Linköping University, Linköping SE-58183, Sweden

Weimin M. Chen – Department of Physics, Chemistry and Biology, Linköping University, Linköping SE-58183, Sweden; orcid.org/0000-0002-6405-9509

Complete contact information is available at: <https://pubs.acs.org/doi/10.1021/acs.jpcc.2c07493>

Notes

The authors declare no competing financial interest.

■ ACKNOWLEDGMENTS

This work was financially supported by Knut and Alice Wallenberg Foundation (Dnr. KAW 2019.0082), the Swedish Energy Agency (Dnr 48758-1), and the Swedish Government Strategic Research Area in Materials Science on Functional Materials at Linköping University (Faculty Grant SFO-Mat-LiU No. 2009-00971). G.Y.R. is grateful to the Swedish Foundation for Strategic Research for the financial support (Dnr. UKR22-0029). S.I.S. acknowledges the support from Swedish Research Council (VR) (Project No. 2019-05551) and the ERC (synergy grant FAST-CORR project 854843). The computations were enabled by resources provided by the Swedish National Infrastructure for Computing (SNIC), partially funded by the Swedish Research Council through grant agreement no. 2018-05973.

■ REFERENCES

- (1) Sahli, F.; Werner, J.; Kamino, B. A.; Brauninger, M.; Monnard, R.; Paviet-Salomon, B.; Barraud, L.; Ding, L.; Leon, J. J. D.; Sacchetto, D.; et al. Fully Textured Monolithic Perovskite/Silicon Tandem Solar Cells with 25.2% Power Conversion Efficiency. *Nat. Mater.* **2018**, *17*, 820–826.
- (2) Leijtens, T.; Bush, K. A.; Prasanna, R.; McGehee, M. D. Opportunities and Challenges for Tandem Solar Cells Using Metal Halide Perovskite Semiconductors. *Nat. Energy* **2018**, *3*, 828–838.
- (3) Sutherland, B. R.; Sargent, E. H. Perovskite Photonic Sources. *Nat. Photonics* **2016**, *10*, 295–302.
- (4) Stranks, S. D.; Snaith, H. J. Metal-Halide Perovskites for Photovoltaic and Light-Emitting Devices. *Nat. Nanotechnol.* **2015**, *10*, 391–402.
- (5) Liu, X. K.; Xu, W.; Bai, S.; Jin, Y.; Wang, J.; Friend, R. H.; Gao, F. Metal Halide Perovskites for Light-Emitting Diodes. *Nat. Mater.* **2021**, *20*, 10–21.
- (6) Shamsi, J.; Urban, A. S.; Imran, M.; De Trizio, L.; Manna, L. Metal Halide Perovskite Nanocrystals: Synthesis, Post-Synthesis Modifications, and Their Optical Properties. *Chem. Rev.* **2019**, *119*, 3296–3348.

- (7) Babayigit, A.; Ethirajan, A.; Muller, M.; Conings, B. Toxicity of Organometal Halide Perovskite Solar Cells. *Nat. Mater.* **2016**, *15*, 247–251.
- (8) Manser, J. S.; Saidaminov, M. I.; Christians, J. A.; Bakr, O. M.; Kamat, P. V. Making and Breaking of Lead Halide Perovskites. *Acc. Chem. Res.* **2016**, *49*, 330–338.
- (9) Giustino, F.; Snaith, H. J. Toward Lead-Free Perovskite Solar Cells. *ACS Energy Lett.* **2016**, *1*, 1233–1240.
- (10) Slavney, A. H.; Hu, T.; Lindenberg, A. M.; Karunadasa, H. I. A Bismuth-Halide Double Perovskite with Long Carrier Recombination Lifetime for Photovoltaic Applications. *J. Am. Chem. Soc.* **2016**, *138*, 2138–2141.
- (11) Greul, E.; Petrus, M. L.; Binek, A.; Docampo, P.; Bein, T. Highly Stable, Phase Pure $\text{Cs}_2\text{AgBiBr}_6$ Double Perovskite Thin Films for Optoelectronic Applications. *J. Mater. Chem. A* **2017**, *5*, 19972–19981.
- (12) Igbari, F.; Wang, R.; Wang, Z. K.; Ma, X. J.; Wang, Q.; Wang, K. L.; Zhang, Y.; Liao, L. S.; Yang, Y. Composition Stoichiometry of $\text{Cs}_2\text{AgBiBr}_6$ Films for Highly Efficient Lead-Free Perovskite Solar Cells. *Nano Lett.* **2019**, *19*, 2066–2073.
- (13) Wu, B.; Ning, W. H.; Xu, Q.; Manjappa, M.; Feng, M. J.; Ye, S. Y.; Fu, J. H.; Lie, S.; Yin, T. T.; Wang, F.; et al. Strong Self-Trapping by Deformation Potential Limits Photovoltaic Performance in Bismuth Double Perovskite. *Sci. Adv.* **2021**, *7*, eabd3160.
- (14) Pan, W. C.; Wu, H. D.; Luo, J. J.; Deng, Z. Z.; Ge, C.; Chen, C.; Jiang, X. W.; Yin, W. J.; Niu, G. D.; Zhu, L. J.; et al. $\text{Cs}_2\text{AgBiBr}_6$ Single-Crystal X-Ray Detectors with a Low Detection Limit. *Nat. Photonics* **2017**, *11*, 726–732.
- (15) Luo, J. J.; Wang, X. M.; Li, S. R.; Liu, J.; Guo, Y. M.; Niu, G. D.; Yao, L.; Fu, Y. H.; Gao, L.; Dong, Q. S.; et al. Efficient and Stable Emission of Warm-White Light from Lead-Free Halide Double Perovskites. *Nature* **2018**, *563*, 541–545.
- (16) Volonakis, G.; Haghighirad, A. A.; Milot, R. L.; Sio, W. H.; Filip, M. R.; Wenger, B.; Johnston, M. B.; Herz, L. M.; Snaith, H. J.; Giustino, F. $\text{Cs}_2\text{InAgCl}_6$: A New Lead-Free Halide Double Perovskite with Direct Band Gap. *J. Phys. Chem. Lett.* **2017**, *8*, 772–778.
- (17) Du, K. Z.; Meng, W. W.; Wang, X. M.; Yan, Y. F.; Mitzi, D. B. Bandgap Engineering of Lead-Free Double Perovskite $\text{Cs}_2\text{AgBiBr}_6$ through Trivalent Metal Alloying. *Angew. Chem., Int. Ed.* **2017**, *56*, 8158–8162.
- (18) Ning, W.; Gao, F. Structural and Functional Diversity in Lead-Free Halide Perovskite Materials. *Adv. Mater.* **2019**, *31*, 1900326.
- (19) Meng, W. W.; Wang, X. M.; Xiao, Z. W.; Wang, J. B.; Mitzi, D. B.; Yan, Y. F. Parity-Forbidden Transitions and Their Impact on the Optical Absorption Properties of Lead-Free Metal Halide Perovskites and Double Perovskites. *J. Phys. Chem. Lett.* **2017**, *8*, 2999–3007.
- (20) Xue, J.; Wang, Z. Y.; Comstock, A.; Wang, Z. Y.; Sung, H. H. Y.; Williams, I. D.; Sun, D. L.; Liu, J. W.; Lu, H. P. Chemical Control of Magnetic Ordering in Hybrid Fe-Cl Layered Double Perovskites. *Chem. Mater.* **2022**, *34*, 2813–2823.
- (21) Ning, W.; Bao, J.; Puttison, Y.; Moro, F.; Kobera, L.; Shiono, S.; Wang, L.; Ji, F.; Cuartero, M.; Kawaguchi, S.; et al. Magnetizing Lead-Free Halide Double Perovskites. *Sci. Adv.* **2020**, *6*, eabb5381.
- (22) Li, W. Z.; Rahman, N. U.; Xian, Y. M.; Yin, H.; Bao, Y. K.; Long, Y.; Yuan, S. Y.; Zhang, Y. Y.; Yuan, Y. X.; Fan, J. D. Regulation of the Order-Disorder Phase Transition in a $\text{Cs}_2\text{NaFeCl}_6$ Double Perovskite Towards Reversible Thermochromic Application. *J. Semicond.* **2021**, *42*, 072202.
- (23) Xian, Y.; Yin, H.; Bao, Y.; Xiao, Y.; Yuan, S.; Rahman, N. U.; Yuan, Y.; Zhang, Y.; Meng, X.; Jin, S.; et al. Engineered Electronic Structure and Carrier Dynamics in Emerging $\text{Cs}_2\text{Ag}_x\text{Na}_{1-x}\text{FeCl}_6$ Perovskite Single Crystals. *J. Phys. Chem. Lett.* **2020**, *11*, 9535–9542.
- (24) Yaffe, O.; Guo, Y.; Tan, L. Z.; Egger, D. A.; Hull, T.; Stoumpos, C. C.; Zheng, F.; Heinz, T. F.; Kronik, L.; Kanatzidis, M. G.; et al. Local Polar Fluctuations in Lead Halide Perovskite Crystals. *Phys. Rev. Lett.* **2017**, *118*, 136001.
- (25) Klarbring, J.; Hellman, O.; Abrikosov, I. A.; Simak, S. I. Anharmonicity and Ultralow Thermal Conductivity in Lead-Free Halide Double Perovskites. *Phys. Rev. Lett.* **2020**, *125*, 045701.
- (26) Yamada, Y.; Kanemitsu, Y. Electron-Phonon Interactions in Halide Perovskites. *NPG Asia Mater.* **2022**, *14*, 1–15.
- (27) Steele, J. A.; Puech, P.; Keshavarz, M.; Yang, R.; Banerjee, S.; Debroye, E.; Kim, C. W.; Yuan, H.; Heo, N. H.; Vanacken, J.; et al. Giant Electron-Phonon Coupling and Deep Conduction Band Resonance in Metal Halide Double Perovskite. *ACS Nano* **2018**, *12*, 8081–8090.
- (28) Zelewski, S. J.; Urban, J. M.; Surrente, A.; Maude, D. K.; Kuc, A.; Schade, L.; Johnson, R. D.; Dollmann, M.; Nayak, P. K.; Snaith, H. J.; et al. Revealing the Nature of Photoluminescence Emission in the Metal-Halide Double Perovskite $\text{Cs}_2\text{AgBiBr}_6$. *J. Mater. Chem. C* **2019**, *7*, 8350–8356.
- (29) Zhang, H.; Debroye, E.; Zheng, W.; Fu, S.; Virgilio, L. D.; Kumar, P.; Bonn, M.; Wang, H. I. Highly Mobile Hot Holes in $\text{Cs}_2\text{AgBiBr}_6$ Double Perovskite. *Sci. Adv.* **2021**, *7*, eabj9066.
- (30) Yang, J. X.; Zhang, P.; Wei, S. H. Band Structure Engineering of $\text{Cs}_2\text{AgBiBr}_6$ Perovskite through Order Disordered Transition: A First-Principle Study. *J. Phys. Chem. Lett.* **2018**, *9*, 31–35.
- (31) Yuan, W. N.; Niu, G. D.; Xian, Y. M.; Wu, H. D.; Wang, H. M.; Yin, H.; Liu, P.; Li, W. Z.; Fan, J. D. In Situ Regulating the Order-Disorder Phase Transition in $\text{Cs}_2\text{AgBiBr}_6$ Single Crystal toward the Application in an X-Ray Detector. *Adv. Funct. Mater.* **2019**, *29*, 1900234.
- (32) Kresse, G.; Furthmüller, J. Efficiency of Ab-Initio Total Energy Calculations for Metals and Semiconductors Using a Plane-Wave Basis Set. *Comput. Mater. Sci.* **1996**, *6*, 15–50.
- (33) Kresse, G.; Joubert, D. From Ultrasoft Pseudopotentials to the Projector Augmented-Wave Method. *Phys. Rev. B* **1999**, *59*, 1758–1775.
- (34) Kresse, G.; Furthmüller, J. Efficient Iterative Schemes for Ab Initio Total-Energy Calculations Using a Plane-Wave Basis Set. *Phys. Rev. B* **1996**, *54*, 11169–11186.
- (35) Perdew, J. P.; Ruzsinszky, A.; Csonka, G. I.; Vydrov, O. A.; Scuseria, G. E.; Constantin, L. A.; Zhou, X. L.; Burke, K. Restoring the Density-Gradient Expansion for Exchange in Solids and Surfaces. *Phys. Rev. Lett.* **2008**, *100*, 136406.
- (36) Dudarev, S. L.; Botton, G. A.; Savrasov, S. Y.; Humphreys, C. J.; Sutton, A. P. Electron-Energy-Loss Spectra and the Structural Stability of Nickel Oxide: An LSDA+U Study. *Phys. Rev. B* **1998**, *57*, 1505–1509.
- (37) Masuki, R.; Nomoto, T.; Arita, R.; Tadano, T. Anharmonic Gruneisen Theory Based on Self-Consistent Phonon Theory: Impact of Phonon-Phonon Interactions Neglected in the Quasiharmonic Theory. *Phys. Rev. B* **2022**, *105*, 064112.
- (38) Tadano, T.; Gohda, Y.; Tsuneyuki, S. Anharmonic Force Constants Extracted from First-Principles Molecular Dynamics: Applications to Heat Transfer Simulations. *J. Phys-Condens Mat* **2014**, *26*, 225402.
- (39) Tadano, T.; Tsuneyuki, S. Self-Consistent Phonon Calculations of Lattice Dynamical Properties in Cubic SrTiO_3 with First-Principles Anharmonic Force Constants. *Phys. Rev. B* **2015**, *92*, 054301.
- (40) Sun, Z.; Chen, X.; Yin, W. Comprehensive First-Principles Studies on Phase Stability of Copper-Based Halide Perovskite Derivatives ACu_mX_n (A = Rb and Cs; X = Cl, Br, and I). *J. Semicond.* **2020**, *41*, 052201.
- (41) Iliev, M. N.; Abrashev, M. V.; Litvinchuk, A. P.; Hadjiev, V. G.; Guo, H.; Gupta, A. Raman Spectroscopy of Ordered Double Perovskite $\text{La}_2\text{CoMnO}_6$ Thin Films. *Phys. Rev. B* **2007**, *75*, 104118.
- (42) Gaune-Escard, M. *Molten Salts: From Fundamentals to Applications*; Springer Science & Business Media: Dordrecht, 2002; Vol. 52.
- (43) Cohen, A.; Brenner, T. M.; Klarbring, J.; Sharma, R.; Fabini, D. H.; Korobko, R.; Nayak, P. K.; Hellman, O.; Yaffe, O. Diverging Expressions of Anharmonicity in Halide Perovskites. *Adv. Mater.* **2022**, *34*, 2107932.
- (44) Martin, T. P. Multiple-Order Raman-Scattering by a Localized Mode. *Phys. Rev. B* **1976**, *13*, 3617–3622.
- (45) Iaru, C. M.; Brodu, A.; van Hoof, N. J. J.; Ter Huurne, S. E. T.; Buhot, J.; Montanarella, F.; Buhbut, S.; Christianen, P. C. M.;

Vanmaekelbergh, D.; de Mello Donega, C.; et al. Frohlich Interaction Dominated by a Single Phonon Mode in CsPbBr₃. *Nat. Commun.* **2021**, *12*, 5844.

(46) Peter, Y.; Cardona, M. *Fundamentals of Semiconductors: Physics and Materials Properties*; Springer Science & Business Media: Dordrecht, 2010.

(47) Xu, K.-X.; Lai, J.-M.; Gao, Y.-F.; Song, F.; Sun, Y.-J.; Tan, P.-H.; Zhang, J. High-Order Raman Scattering Mediated by Self-Trapped Exciton in Halide Double Perovskite. *Phys. Rev. B* **2022**, *106*, 085205.

(48) Perebeinos, V.; Allen, P. B. Multiphonon Resonant Raman Scattering Predicted in LaMnO₃ from the Franck-Condon Process Via Self-Trapped Excitons. *Phys. Rev. B* **2001**, *64*, 085118.

(49) Urbach, F. The Long-Wavelength Edge of Photographic Sensitivity and of the Electronic Absorption of Solids. *Phys. Rev.* **1953**, *92*, 1324.

(50) Cody, G. D.; Tiedje, T.; Abeles, B.; Brooks, B.; Goldstein, Y. Disorder and the Optical-Absorption Edge of Hydrogenated Amorphous-Silicon. *Phys. Rev. Lett.* **1981**, *47*, 1480–1483.

(51) Sadigh, B.; Erhart, P.; Aberg, D.; Trave, A.; Schwegler, E.; Bude, J. First-Principles Calculations of the Urbach Tail in the Optical Absorption Spectra of Silica Glass. *Phys. Rev. Lett.* **2011**, *106*, 027401.

(52) Greeff, C. W.; Glyde, H. R. Anomalous Urbach Tail in GaAs. *Phys. Rev. B Condens Matter* **1995**, *51*, 1778–1783.

(53) Bonalde, I.; Medina, E.; Rodriguez, M.; Wasim, S. M.; Marin, G.; Rincon, C.; Rincon, A.; Torres, C. Urbach Tail, Disorder, and Localized Modes in Ternary Semiconductors. *Phys. Rev. B* **2004**, *69*, 195201.

(54) Ayik, C.; Studenyak, I.; Kranjec, M.; Kurik, M. Urbach Rule in Solid State Physics. *Int. J. Opt. Appl.* **2014**, *4*, 76–83.

(55) Tao, W.; Zhang, C.; Zhou, Q.; Zhao, Y.; Zhu, H. Momentarily Trapped Exciton Polaron in Two-Dimensional Lead Halide Perovskites. *Nat. Commun.* **2021**, *12*, 1400.

(56) Song, K.; Williams, R. T. Self-Trapped Excitons. In *Springer Series in Solid-State Sciences*, 2nd ed.; Cardona, M., Ed. Springer-Verlag: Berlin, 1995; Vol. 105, p 25.

(57) Sumi, H.; Toyozawa, Y. Urbach-Martienssen Rule and Exciton Trapped Momentarily by Lattice Vibrations. *J. Phys. Soc. Jpn.* **1971**, *31*, 342–358.

(58) Connor, B. A.; Leppert, L.; Smith, M. D.; Neaton, J. B.; Karunadasa, H. I. Layered Halide Double Perovskites: Dimensional Reduction of Cs₂AgBiBr₆. *J. Am. Chem. Soc.* **2018**, *140*, 5235–5240.

(59) Fröhlich, H. Electrons in Lattice Fields. *Adv. Phys.* **1954**, *3*, 325–361.

(60) Frost, J. M. Calculating Polaron Mobility in Halide Perovskites. *Phys. Rev. B* **2017**, *96*, 195202.

(61) Buizza, L. R.; Herz, L. M. Polarons and Charge Localization in Metal-Halide Semiconductors for Photovoltaic and Light-Emitting Devices. *Adv. Mater.* **2021**, *33*, 2007057.

(62) Manna, D.; Kangsabanik, J.; Das, T. K.; Das, D.; Alam, A.; Yella, A. Lattice Dynamics and Electron-Phonon Coupling in Lead-Free Cs₂AgIn_{1-x}Bi_xCl₆ Double Perovskite Nanocrystals. *J. Phys. Chem. Lett.* **2020**, *11*, 2113–2120.

Recommended by ACS

Indirect Bandgap Emission of the Metal Halide Perovskite FAPbI₃ at Low Temperatures

Cong Tao, Jianpu Wang, et al.

APRIL 13, 2023

THE JOURNAL OF PHYSICAL CHEMISTRY LETTERS

READ 

Deciphering the Relevance of Quantum Confinement in the Optoelectronics of CsPbBr₃ Perovskite Nanostructures

Leepsa Mishra, Manas Kumar Sarangi, et al.

MARCH 09, 2023

THE JOURNAL OF PHYSICAL CHEMISTRY LETTERS

READ 

Elucidating the Structure–Property Relationship and Ultrafast Exciton/Charge Carrier Dynamics of Layered Cs₄CuSb₂Cl₁₂ Double-Perovskite Microcrystals

Samita Mishra, Arijit K. De, et al.

JANUARY 19, 2023

THE JOURNAL OF PHYSICAL CHEMISTRY C

READ 

Luminescence Enhancement of CsMnBr₃ Nanocrystals through Heterometallic Doping

Yaocang Li, Zhengtao Deng, et al.

FEBRUARY 16, 2023

THE JOURNAL OF PHYSICAL CHEMISTRY LETTERS

READ 

Get More Suggestions >